

Two-dimensional orbital-obstructed insulators with higher-order band topology

Olga Arroyo-Gascón^{†*}

Nanotechnology Group, USAL – Nanolab, University of Salamanca, 37008, Salamanca, Spain

Sergio Bravo[†] and Mónica Pacheco

Departamento de Física, Universidad Técnica Federico Santa María, Casilla 110-V, Valparaíso, Chile

Leonor Chico

*GISC, Departamento de Física de Materiales, Facultad de Ciencias Físicas,
Universidad Complutense de Madrid, E-28040 Madrid, Spain*

(Dated: August 19, 2025)

Obstructed atomic phases, with their realizations in systems of diverse dimensionality, have recently arisen as one of the topological states with greatest potential to show higher-order phenomena. In this work we report a special type of obstruction, known as orbital-mediated atomic obstruction, in monolayers of materials with crystalline symmetry described by the space group $P\bar{3}m1$. By means of a minimal tight-binding model and first-principles calculations, we show that this obstructed phase is related to the mismatch of the charge centers coming from the atomic limit with respect to the centers that are obtained from a reciprocal space description. Although we find atomic limits that correspond with occupied atomic sites, orbital-mediated atomic obstruction requires the presence of orbitals that have no support in real space. In order to demonstrate the nontrivial character of the obstruction, we confirm the presence of a filling anomaly for finite geometries that is directly associated with the bulk configuration, and discuss the role of the boundary states and their underlying mechanism. Several material examples are presented to illustrate the ubiquity of these nontrivial responses and, in turn, to discuss the differences related to the particular ground state configuration. In addition, we perform a survey of materials and elaborate a list of candidate systems which will host this obstructed phase in monolayer form.

I. INTRODUCTION

Modern materials science has witnessed a breakthrough due to the inclusion and adaptation of notions from topology as key tools for the analysis and discovery of new phenomena. This approach has led to the establishment of novel phases in materials with paradigmatic examples such as topological insulators, topological semimetals and topological superconductors [1–3]. In recent years, this topological description has been extended to include not only three- and two-dimensional systems that exhibit anomalous surface or edge states, respectively, but also higher-order states. A n -th order d -dimensional topological phase hosts $d - n$ -dimensional states. Therefore, a new variety of symmetry-protected states have emerged, generating great interest in their potential applications [4–7].

Hand in hand with these discoveries goes the theoretical description and classification of all different topological phases. Topological Quantum Chemistry (TQC) theory and the associated symmetry indicators formalisms stand out as one of the most useful tools for analyzing crystalline materials [8–14]. Within this setting, the band topology of any material can be analyzed in a straightforward process and their diverse topological features can be identified.

In this work, we use the TQC framework to search for higher-order effects in two-dimensional systems. We focus on materials for which the set of valence bands can be described by Wannier functions, implying a well-defined atomic limit [8, 15]. In such scenario, the valence band set can be expressed as a linear combination of the so-called elementary band representations (EBRs) [8, 9, 15]. These EBRs correspond to the band representations that will be induced in momentum space by different orbitals located at specific (maximal) Wyckoff positions (WPs) in real space [9]. WPs are said to be maximal if the symmetry operations that leave them invariant (dubbed the site-symmetry group) constitute a subgroup of the space group of the material, but are not a subgroup of any other site-symmetry groups [9, 15]. In terms of strong topology, these systems are termed as trivial insulators. However, since the map from real to momentum space is not one-to-one, there can be atomic insulators whose valence band manifold can only be described including EBRs that are induced from WPs that do not correspond to the atomic positions in the crystal [8].

Such materials, in which the valence bands contain one or more unavoidable EBRs coming from an unoccupied WP, are denoted as obstructed atomic insulators (OAI) [8, 16]. A second kind of obstruction is realized when, although all the EBRs describing the valence band come from occupied WPs, there is a mismatch between the expected band representations that are induced by the specific orbitals and the actual EBRs that the material contains. These insulators are known as orbital-obstructed

* o.arroyo.gascon@usal.es

† These two authors contributed equally.

atomic insulators (OOAI) or unconventional atomic insulators [17, 18].

The previous general definitions yield a more elaborate classification of atomic insulators. In particular, in two-dimensional systems, corner states and charges have been reported in OAI material candidates since 2019 [19, 20], allowing for the discovery of new topological phenomena related to higher-order responses. Less studied are the OOAI, which have been previously reported in Refs. [21–23] and associated, for example, with obstructed edge states and superconducting corner states.

In this work, we focus on a family of two-dimensional materials in monolayer form, with spatial symmetry described by space group (SG) $P\bar{3}m1$ (No. 164) and with formula MX_2 , where M can be in general a metal and X represents a chalcogen or halogen atom. These monolayers have been widely studied and many of them are experimentally feasible, such as compounds with $M=\text{Zr, Ni, Sn, Pt, Pd}$ or Pb [24–33]. Besides, several theoretical proposals have been reported in computational databases [34, 35]. Our analysis uncovers an OOAI phase in this type of materials, for which we propose a second-order bulk-boundary correspondence associated with this obstructed state that is identified in finite geometries by an electron filling anomaly.

The article is organized as follows. In Section II, we review SG No. 164 from a TQC perspective; in Section III, we propose a minimal tight-binding model that obeys the symmetries of that SG, and discuss the emergence of a filling anomaly, corner and edge states within that setting. In Section IV, we present material realizations to the effects outlined in the previous sections, introducing three representative materials that reflect the different scenarios previously analyzed. Section V discusses the overall findings and significance of this work.

II. STRUCTURAL AND SYMMETRY PROPERTIES OF SPACE GROUP $P\bar{3}m1$ MATERIALS

The materials of interest in this work have a lattice structure with unit cell depicted in Fig. 1, where the lattice vectors for the two periodic directions (defined in the xy plane) are expressed as $\mathbf{a} = a\hat{x}$ and $\mathbf{b} = -(1/2)a\hat{x} + (\sqrt{3}/2)a\hat{y}$, with a being the lattice parameter. The symmetries of this lattice are described by the layer version of the SG $P\bar{3}m1$ (layer group No. 72), with twelve symmetries, which is generated by spatial inversion, a threefold symmetry of $2\pi/3$ about the z -axis perpendicular to the monolayer plane, and a twofold rotation around an in-plane axis [36]. We also assume that time-reversal symmetry is preserved in all cases considered in this work.

The structures with formula MX_2 can be generically described under this SG by the identification of the WP for each type of atom. The M atom located at the origin of the unit cell corresponds to the $1a$ WP, and the pair

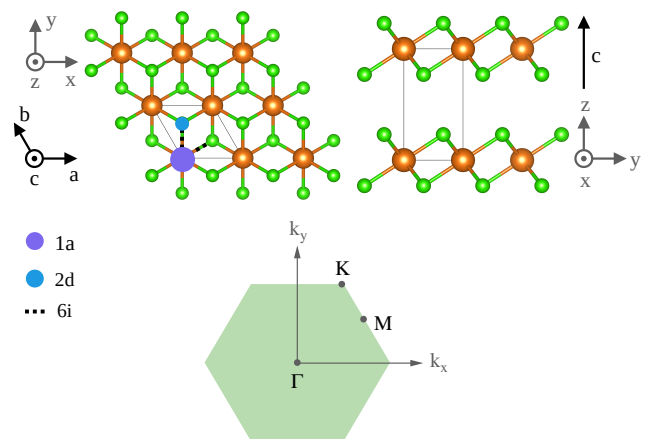


FIG. 1. Top panel: crystal structure of a SG No. 164 unit cell, from a top (left panel) and side (right panel) view. The $1a$ and $2d$ WPs are indicated as blue and orange highlighted atoms in the top left panel, and the $6i$ WP as black dashed lines. Bottom panel: monolayer Brillouin zone.

of X atoms compose the $2d$ WP. This last WP implies that the structure has a buckled configuration (see Fig. 1). The occupied WPs play a key role in the symmetry description in real and momentum space.

As time-reversal symmetry and spatial inversion are both present, all energy bands will be twofold degenerate along the entire Brillouin zone (BZ). The relevant high-symmetry points of the BZ are Γ , M and K . Since spin-orbit coupling is also considered, double space group irreducible representations (irreps) are considered [37]. Note that both SG No. 164 and layer group No. 72 share the same irreps at these high-symmetry points, so a one-to-one correspondence can be established. The monolayer BZ along with their HSPs is shown in Fig.1. In this scenario, bands are at most twofold degenerate, which allows us to study each twofold degenerate band separately. Another important ingredient that is derived from real space symmetry is the type of band representation that atomic orbitals induce in momentum space. Although we use double-valued irreps, analyzing the symmetry features of the atomic orbitals allows to relate the band representation (BR) with the inducing spinful orbitals at the occupied atomic sites.

For SG No. 164 we need to consider each occupied WP separately. For WP $1a$, the local symmetry is described by the site-symmetry group (SSG) $P\bar{3}m1$, the complete point group of the SG [36, 38, 39]. Under this local symmetry, the crystalline field produces atomic level splittings that group the atomic levels in sets with a maximal twofold degeneracy [40]. In addition, as inversion is present in the SSG, p orbitals transform differently from d and s orbitals. Therefore, we can identify the irreps that label the BR for each set of orbitals, as summarized in Table I. The same process can be repeated for the $2d$ WP, whose SSG is $P\bar{3}m1$. In this case no inversion is present, and then there is no distinction of atomic orbitals related

to spatial parity. Thus, the orbitals located at this WP are classified mainly by the degeneracy resulting from the crystal field splitting. A summary of the BRs that can be obtained from atomic orbitals located at this WP is also presented in Table I.

The data in Table I will be useful for characterizing the OOAI phase, and is also the starting point to construct a minimal tight-binding model that illustrates this topological phase.

III. MINIMAL TIGHT-BINDING DESCRIPTION OF THE OOAI STATE

To show how the orbital-induced obstruction arises in materials with SG No. 164, we build a tight-binding model by decorating the $1a$ and $2d$ WPs with atomic orbitals. The particular choice of the orbitals has no effect on the realization of the obstruction. Thereby, we place a single (spinful) orbital that transforms as \bar{E}_{1g} at $1a$, and one (spinful) orbital at each site of the $2d$ WP, which transforms as \bar{E}_1 (see Table I for details on the BRs). This yields a total of six orbitals, which in turn conform a six-band model in reciprocal space. In the following, we use a state basis ordered as $\{|\psi_{1a}, \uparrow\rangle, |\psi_{1a}, \downarrow\rangle, |\psi_{2d}^A, \uparrow\rangle, |\psi_{2d}^A, \downarrow\rangle, |\psi_{2d}^B, \uparrow\rangle, |\psi_{2d}^B, \downarrow\rangle\}$.

$$H_{2d} = \begin{pmatrix} \epsilon_{2d} + F(r_1, r_4) & G(r_3) & L(s_1) & 0 \\ G^*(r_3) & \epsilon_{2d} + F(-r_1, r_4) & 0 & L(s_1) \\ L^*(s_1) & 0 & \epsilon_{2d} + F(-r_1, r_4) & G(-r_3) \\ 0 & L^*(s_1) & G^*(-r_3) & \epsilon_{2d} + F(r_1, r_4) \end{pmatrix}. \quad (3)$$

Here, ϵ_{2d} is the onsite energy for orbitals at the $2d$ WP and r_1 parameterizes the spinless interaction, while r_3 and r_4 parameterize, respectively, the spin-flip and the spin-conserving spin-orbit couplings. For its part, s_1 parameterizes the interaction between different sites of the $2d$ WP, that is, between the top and bottom atoms of the monolayer. Finally, the block describing the inter-sublattice interaction, $H_{1a,2d}$, is given by

$$H_{1a,2d} = \begin{pmatrix} L(t_2) & \tilde{M}(t_1) & L^*(-t_2) & T(t_1) \\ M(t_1) & L(t_2) & \tilde{T}(t_1) & L^*(-t_2) \end{pmatrix}, \quad (4)$$

where t_1 and t_2 parameterize, respectively, the spin-flip and spin-conserving interactions between the orbitals located at $1a$ and $2d$ WPs. The explicit form of the functions F, G, L, M, \tilde{M}, T and \tilde{T} is reported in the Appendix. The previous model is solved numerically to obtain the band structure for particular values of the parameters. For convenience, these values are chosen such that no band inversion is produced, which means that no strong topological band is realized. This has no impact on the results obtained.

In order to clarify the forthcoming discussion, which

The subscript of state ψ denotes the WP at which the orbital is located and, for the $2d$ states, the superscript distinguishes between the two sites that compose this WP. The arrows indicate the spin character of the state, considering as the basis the two spin states for a quantization axis along the z direction.

By including spin-orbit coupling, we construct with the aid of the method discussed in Ref. [41] a Hamiltonian that respects all the spatial transformations along with time-reversal symmetry. The formulation in block form in momentum space will be

$$H = \begin{pmatrix} H_{1a} & H_{1a,2d} \\ H_{1a,2d}^* & H_{2d} \end{pmatrix}. \quad (1)$$

The H_{1a} block, which describes the interaction between the $1a$ sites, is given by (for simplicity we omit the explicit momentum dependence in all the following functions)

$$H_{1a} = \begin{pmatrix} \epsilon_{1a} + F(0, r_2) & 0 \\ 0 & \epsilon_{1a} + F(0, r_2) \end{pmatrix}, \quad (2)$$

where ϵ_{1a} is the onsite energy for orbitals at $1a$ WP and r_2 is a real parameter to quantify the $1a, 1a$ coupling. The interaction between the $2d$ sites, H_{2d} , will be expressed as

relates the model to the material realizations, we will distinguish between two regimes based on the relative magnitudes of the onsite energies: A) $\epsilon_{2d} < \epsilon_{1a}$ and B) $\epsilon_{1a} < \epsilon_{2d}$. Throughout this section, we will assume a bulk filling of $2/3$, that is, four of the six bands are completely filled. An example of a band structure for this setting is presented in Fig. 2a.

A. Case $\epsilon_{2d} < \epsilon_{1a}$

As mentioned in the introduction, following TQC, an atomic insulator can always be described as a linear combination of EBRs induced from maximal WPs [8, 9]. This implies that, in the atomic limit, we could order the bands according to the onsite energy of the set of orbitals. Therefore, if we consider $\epsilon_{2d} < \epsilon_{1a}$, the four bands induced from the $2d$ WP will be the lowest energy bands in the system. The same picture can be maintained if we turn on the hopping interactions of the model, provided that no gap closures occur with the upper bands.

According to the $2/3$ fixed filling we are working with,

WP	Orbitals	Irreps induced at HSPs	EBR decomposition
1a	$(s \text{ or } d_{z^2}) \otimes (\uparrow\rangle, \downarrow\rangle)$	$\bar{\Gamma}_8 - \bar{M}_3\bar{M}_4 - \bar{K}_6$	$\bar{E}_{1g}(1a)$
1a	$(p_x, p_y) \otimes (\uparrow\rangle, \downarrow\rangle)$	$\bar{\Gamma}_6\bar{\Gamma}_7 \oplus \bar{\Gamma}_9 - 2\bar{M}_5\bar{M}_6 - \bar{K}_4\bar{K}_5 \oplus \bar{K}_6$	$\bar{E}_{1u}(1a) \oplus {}^1\bar{E}_u {}^2\bar{E}_u(1a)$
1a	$p_z \otimes (\uparrow\rangle, \downarrow\rangle)$	$\bar{\Gamma}_9 - \bar{M}_5\bar{M}_6 - \bar{K}_6$	$\bar{E}_{1u}(1a)$
1a	$((d_{xy}, d_{yz}) \text{ or } (d_{xy}, d_{x^2-y^2})) \otimes (\uparrow\rangle, \downarrow\rangle)$	$\bar{\Gamma}_4\bar{\Gamma}_5 \oplus \bar{\Gamma}_8 - 2\bar{M}_3\bar{M}_4 - \bar{K}_4\bar{K}_5 \oplus \bar{K}_6$	$\bar{E}_{1g}(1a) \oplus {}^1\bar{E}_g {}^2\bar{E}_g(1a)$
2d	$(s \text{ or } p_z \text{ or } d_{z^2}) \otimes (\uparrow\rangle, \downarrow\rangle)$	$\bar{\Gamma}_8 \oplus \bar{\Gamma}_9 - \bar{M}_3\bar{M}_4 \oplus \bar{M}_5\bar{M}_6 - \bar{K}_4\bar{K}_5 \oplus \bar{K}_6$	$\bar{E}_1(2d)$
2d	$((p_x, p_y) \text{ or } (d_{xy}, d_{yz}) \text{ or } (d_{xy}, d_{x^2-y^2})) \otimes (\uparrow\rangle, \downarrow\rangle)$	$\bar{\Gamma}_4\bar{\Gamma}_5 \oplus \bar{\Gamma}_6\bar{\Gamma}_7 \oplus \bar{\Gamma}_8 \oplus \bar{\Gamma}_9 - 2\bar{M}_3\bar{M}_4 \oplus 2\bar{M}_5\bar{M}_6 - \bar{K}_4\bar{K}_5 \oplus 3\bar{K}_6$	$\bar{E}_1(2d) \oplus {}^1\bar{E}^2\bar{E}(2d)$

TABLE I. Irreducible representations at HSPs induced from atomic orbitals located at the 1a and 2d WP of SG No. 164. The EBR decomposition for each induced set of irreps is presented in the fourth column. Information has been retrieved from BANDREP code in the Bilbao Crystallographic Server [36–39] and adapted for a layer group configuration.

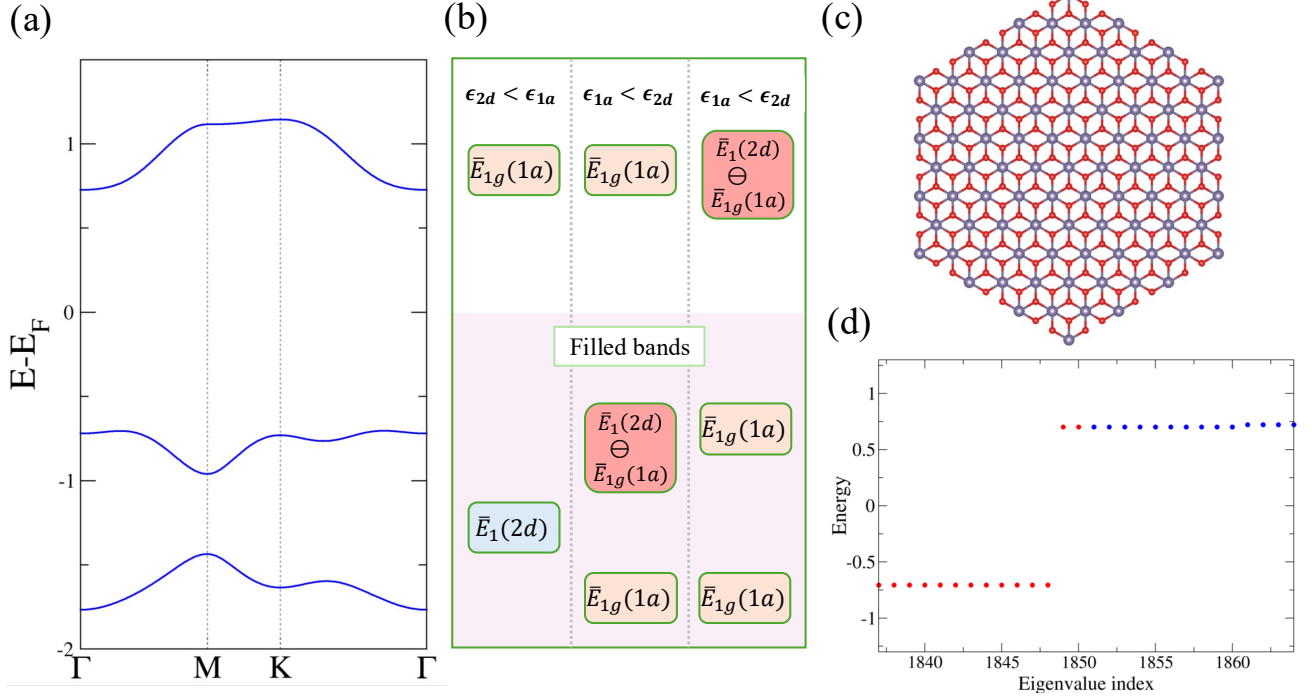


FIG. 2. (a) Schematic band structure for the minimal tight-binding model of Section III. (b) Diagrammatic depiction of the occupied and unoccupied bands of the aforementioned model, highlighting the different three regimes discussed in the text. (c) Hexagonal flake presenting $P\bar{3}m1$ point group geometry, and (d) its corresponding eigenvalue spectra, where the occupied states are colored red.

the four low-lying bands comprise the valence bands of the model and, for the present energy ordering, this set of bands can be described by the EBR $\bar{E}_1(2d)$ (see leftmost panel of Fig. 2b). This EBR is classified as *decomposable* [42], which means that the four-band group will be separated in two sets of twofold degenerated bands. Depending on the value of parameters controlling the interaction between the 2d sites, this EBR can be expressed either as the combination of another EBR and a band with fragile topology [43] or as the combination of two BRs with strong topology [44]. For this particular case, the actual decomposition does not play a role since we consider that the four bands are filled. However, to simplify the discussion on edge states of Section III D we

assume that the decomposition matches that of an EBR plus a fragile band. In order to spot the obstruction, the bulk filling is studied, where there must be 4 electrons in the unit cell. As the 1a and 2d WPs must be occupied, the only possibility that respects the symmetry of the system is to have 2 electrons (and hence also two ions) at the 1a WP and one electron (and one ion) per site of the 2d WP. This configuration is the only possibility with both WPs occupied. However, referring to Table I, the filled valence bands are represented by EBR $\bar{E}_1(2d)$, in disagreement with the aforementioned only possible arrangement in real space which involved 1a and 2d WPs. This effect is called orbital-induced atomic obstruction, and is a topological bulk obstruction to connect different

atomic phases without breaking the underlying symmetries of the system [17, 18].

B. Case $\epsilon_{1a} < \epsilon_{2d}$

If the orbitals at $1a$ are lower in energy than the $2d$ orbitals, the bands induced from the $1a$ WP will be completely filled and the decomposable EBR induced from the $2d$ WP will be half-filled. Following the same procedure as in case A, and setting the last filled band as a fragile band, we end up with a group of four filled bands that is again described by EBR $\bar{E}_1(2d)$, as illustrated in the middle panel of Fig. 2b. Therefore, an orbital obstruction is again achieved. This scenario, with a half-filled EBR, has been previously analyzed in Ref. [22].

There is one more instance within this regime of onsite energy ordering, which is sketched in the rightmost panel of Fig. 2b. If the last filled band is not a fragile band but an EBR, the valence bands of the model turn out to be described by a sum of two EBRs coming from the $1a$ WP, namely, $2\bar{E}_{1g}(1a)$. This scenario also yields an orbital obstruction, since now all charge centers are predicted to be located at $1a$ in momentum space, which is again not consistent with the atomic positions in real space.

Hence, we have presented three kinds of obstructions in this SG, which will show a non-trivial behavior when considering systems of reduced dimensionality.

C. Filling anomaly induced from an OOI phase

The bulk obstruction that is present in these systems can yield anomalous responses in a finite geometry setting. The N sites of such a finite system can be decomposed into a sum of n_{1a} sites that are related to the bulk $1a$ WP, and n_{2d} pairs of sites that can be mapped to the bulk $2d$ WP. Considering the filling of the bulk (4 electrons per unit cell in the model of Section III), we observe that the expected filling for the finite geometry to be gapped is $4n_{2d}$.

On the other hand, if we impose charge neutrality and a symmetric configuration, we end up with a total electronic charge of $2n_{1a} + 2n_{2d}$. In an open system these two values can differ, implying that the system cannot be in a state that is simultaneously gapped, symmetric and charge neutral, and a filling anomaly arises [19, 20, 45, 46]. This reasoning can be generalized to include arbitrary bulk fillings ν and associated $1a$ and $2d$ site-fillings α_{1a} and α_{2d} , respectively; therefore, a filling anomaly appears if $\nu n_{2d} \neq \alpha_{1a}n_{1a} + \alpha_{2d}n_{2d}$. This result is an indicator that relies on finite geometry quantities.

However, the obstruction is a bulk property, and in consequence, the filling anomaly should be predictable from bulk features. In the previously described minimal model, for the case A of onsite energy ordering (see leftmost panel of Fig. 2b), the bulk characterization of the obstruction is very straightforward. Since the complete

set of valence bands at $2/3$ filling can be described by the EBR $\bar{E}_1(2d)$, the (four) electron charge centers should be located at this WP. In contrast, in a symmetric configuration, two charge centers are expected to appear in position $1a$, and the rest in position $2d$. It follows that there is a mismatch of two electrons in the system, which quantifies the anomaly. Therefore, for a generic system the filling anomaly can be predicted through the determination of the number of obstructed states in the system, which is obtained by comparing the predicted charge centers attending to momentum space information against those obtained by analysis of the real-space orbital content.

To illustrate this anomalous behavior, we consider a particular finite configuration corresponding to a hexagonal flake, which preserves point group $\bar{3}m1$ and is presented in Fig. 2c. Using the minimal model and considering case A with the same parameters as those of Fig. 2a, we compute the energy spectra for a hexagonal flake with $N = 1387$ sites. The result is depicted in Fig. 2d for the range of energies where the bulk gap appears; the filled states are highlighted in red. The filling is calculated imposing charge neutrality and a symmetric system, which results in $n_{1a} = 463$ and $n_{2d} = 462$, and a filling of $2 \cdot 463 + 2 \cdot 462 = 1850$. This differs from the filling needed in order to have a gapped configuration, which is $4n_{2d} = 4 \cdot 462 = 1848$. In agreement with the foregoing analysis of the bulk properties, there are two states that cause the filling anomaly.

In the $\epsilon_{1a} < \epsilon_{2d}$ regime (case B), when the EBR induced by $2d$ is partially filled by a fragile band, we also find a similar filling anomaly. Finally, in the case illustrated by the rightmost panel of Fig. 2b, the method to quantify the anomaly outlined above is still applicable, yielding a filling anomaly of two. This last case has not been encountered in the family of materials scoped in this work. In Section IV, examples for cases A ($\epsilon_{2d} < \epsilon_{1a}$) and B ($\epsilon_{1a} < \epsilon_{2d}$) with the fragile band in the filled set will be presented.

Notably, it is worth mentioning that this anomaly does not require the presence of corner states since, albeit it is one of the properties with which second-order topology and other topological phases have been characterized in previous works [19, 20, 47–56], it is not really a necessary condition for its presence [57]. In the following, we will discuss the role of the boundary states in terms of our minimal model.

D. Edge and corner states

The presented minimal model can also describe the most salient qualitative properties of the edge states found in SG No. 164 monolayers. For the sake of brevity, we will focus on one type of border, since we have numerically checked that the other possible configurations do not substantially alter the conclusions. We build a finite ribbon, depicted in Fig. 3a; in this case, the edges are

similar to the boundaries of the flake structure of Fig. 2c. To explore the enabling conditions for the emergence of edge states, we numerically survey the ribbon energy spectra and local density of states at certain energy values as a function of the parameters of the model. We first describe the results for case A ($\epsilon_{2d} < \epsilon_{1a}$) ordering, and then comment on the reverse regime B.

In Fig. 3c we show two exemplary cases that describe the two major possibilities for edge physics. In general, we find that at the tight-binding level, the spin-orbit interaction with spin-flip character between different WPs is key for the generation of isolated-in-energy edge states. The left panel of Fig. 3c illustrates a case when this interaction is strong enough to generate an isolated set of edge states that are located inside the energy gap. For this regime of onsite energies, the evolution of the edge states with respect to the magnitude of the hopping parameter for the above-mentioned interaction indicates that the edge states detach from the upper bands. The origin of these states can be traced to the hybridization process between the $1a$ sublattice and the $2d$ sublattice.

If in a first instance we consider no inter-sublattice interactions, the $2d$ sublattice will present edge states within the lower gap which are due to the decomposable nature of the EBR. These states are gapped edge states which are inherited from a strong topology phase that arises in a high-symmetry planar structure. Once buckling is present, the gapless states become gapped due to the breaking of the in-plane mirror symmetry. However, they retain some of their spatial localization and, independently if they are gapless or gapped, they can hybridize with the upper bands in the model. Once we turn on sublattice interaction, the edge states produced by the $2d$ sublattice are induced by proximity into the $1a$ sublattice, endowing the upper bands with edge states if the interaction is sufficiently strong. This picture is supported by the local density of the wavefunction, as shown in Fig. 3b, where the spatial localization is evident. This calculation is performed at the energy value where the upper edge states reside (0.85 eV, from the left panel of Fig. 3c).

The spin-orbit interaction that produces the isolated edge states has to compete with other interactions in the system that tend to mask the emergence of edge states. The main competing feature is the energy width of the upper bands. This is mainly affected by the intra-sublattice interaction (r_2) between the $1a$ sites, which greatly affects band dispersion; if this interaction is strong enough, no edge states will arise. This is also related with the fact that the edge states induced by spin-orbit coupling in this type of energy ordering stem from the conduction states, and as such, the edge states will be in general near the bottom of the conduction bands. Therefore, the interaction described by the r_2 parameter, which affects the dispersion of the conduction bands, will also affect the apparition of the edge states. This is the case depicted in the right panel of Fig. 3c (see the value of the model parameters in the caption of this figure). In

this scenario, the edge states are completely inside the bulk bands and therefore are not in general protected to be in-gap.

The above discussion illustrates that the edge state physics is independent of the atomic obstruction, and is produced by hybridization and proximity effects. This way, by tuning the inter- and intra-sublattice interactions, the presence of edge states can be in principle controlled in a ribbon geometry. Interestingly, the emergence of in-gap states in the ribbon geometry is directly linked with the occurrence of in-gap corner states: there is a non-protected edge-to-corner correspondence that can be useful to diagnose the presence of corner states solely by the edge spectrum. To further demonstrate this relation, we resort to the finite hexagonal geometry in Fig. 2c, for the cases exposed in Fig. 3c, and compute the charge density for the states that form the filling anomaly. The results are depicted at the lower insets of each panel in Fig 3c, where the presence of corner states is directly linked to the edge states of the ribbon. This further demonstrates that the filling anomaly does not need for the presence of corner states to be established, since in both cases a filling anomaly appears.

When the onsite energy ordering is inverted in case B ($\epsilon_{1a} < \epsilon_{2d}$), the energy gap active at a bulk filling of $2/3$ is the gap coming from the decomposable $2d$ EBR. The edge states in this case correspond to states stemming directly from the gapped decomposable EBR. These states also hybridize with the now lower in energy $1a$ -induced bands, and then the same proximity-induced effect is produced. However, these induced states are now inaccessible due to the filling.

IV. MATERIAL EXAMPLES

MgCl₂

The first selected material is monolayer MgCl₂, where the Mg atoms sit at the $1a$ WP and the Cl atoms form the $2d$ WP. The electronic band structure from first-principles calculations is presented in Fig. 4a, where one of the advantages of this material becomes readily apparent; it has a large bulk band gap (about 5.0 eV for the level of theory used in the first-principles calculations). This is beneficial as it increases the likelihood of observing corner states more clearly.

To probe this, we compute the energy spectrum of a finite hexagonal geometry with the same configuration as in Fig. 2c. The spectrum is plotted in Fig. 4g for the range of energies where the bulk band gap locates, with colored states according to the electronic filling. The large bulk gap also results in a sizable gap in the finite geometry, even for small structures, which enables the corner states to be directly spotted in the spectrum. As expected from time-reversal symmetry and point group symmetry, there are twelve in-gap states in a narrow energy range, and ideally for larger structures, the states

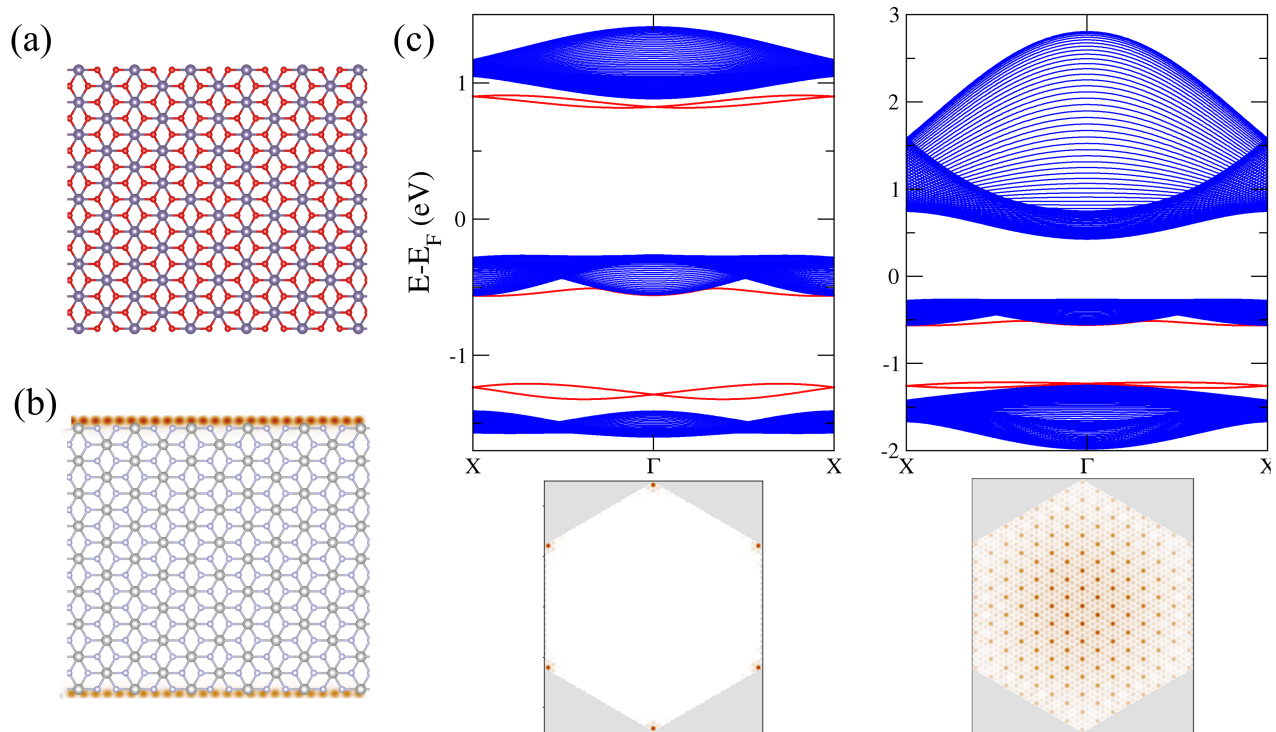


FIG. 3. (a) Finite-width ribbon geometry, with an edge termination analogous to that of the hexagonal flake of Fig. 2c. Edges run horizontally. (b) Local density of states for the ribbon geometry, computed at 0.85 eV, where edge states are expected. (c) Top left panel: band structure for $\epsilon_{1a} = 0.2$, $\epsilon_{2d} = -0.5$, $t_1 = 0.2$, $t_2 = 0.3$, $r_1 = -0.01$, $r_2 = 0.08$, $r_3 = 0.05$, $r_4 = -0.04$, $s_1 = 0.08$. Bottom left panel: corresponding charge density of a hexagonal flake with the same set of parameters. Top right panel: band structure for the same parameters, excepting that now $r_2 = 0.36$. Bottom right panel: corresponding charge density of a hexagonal flake with the set of parameters for the model as in the top right panel.

should be degenerated in energy. The spatial localization of these corner states can be explored with the local density of states as sketched in Fig. 4d. Turning to the filling anomaly, the spectrum of Fig. 4g shows a gapless system with the electronic filling inside the corner states; there must be two filled states within this set and thus the system realizes an obstructed phase, with two obstructed states.

In the following, we analyze the origin of the topological obstruction and the filling anomaly from the bulk band structure perspective. We set as a reference the atomic electronic configurations for each atom in the unit cell: $2s^22p^63s^2$ for Mg and $3s^23p^5$ for Cl. Next, we perform a first-principles ground state calculation to obtain the irreps at the three HSPs in momentum space (see Fig. 1). We present the details of this calculation in the Appendix. If we follow the practice of symmetry indicators, we can form a symmetry data vector \mathbf{B} that summarizes the multiplicities of each irrep for a particular BR [58]. We fix the order of the irreps as $(\bar{\Gamma}_4\bar{\Gamma}_5, \bar{\Gamma}_6\bar{\Gamma}_7, \bar{\Gamma}_8, \bar{\Gamma}_9, \bar{M}_3\bar{M}_4, \bar{M}_5\bar{M}_6, \bar{K}_4\bar{K}_5, \bar{K}_6)$. For MgCl_2 the vector $\mathbf{B}_{\text{MgCl}_2}$ is

$$\mathbf{B}_{\text{MgCl}_2} = (1, 2, 4, 5, 5, 7, 4, 8). \quad (5)$$

This representation allows us to explore the possible decompositions into sums of EBRs. As it is well known,

there can exist several valid decompositions for one band representation. The two starting ingredients are the vector \mathbf{B} and a matrix that summarizes the irrep content for each EBR that the space group has, the so-called EBR matrix, which is denoted simply as \mathbf{EBR} . The explicit form of this matrix for SG $P\bar{3}m1$ is presented in the Appendix. Thereby, the existence of one or more solutions, which we denote as \mathbf{X} , can be compactly formulated as the outcome of the following matrix equation

$$\mathbf{EBR} \cdot \mathbf{X} = \mathbf{B}. \quad (6)$$

In order to explore these solutions, we use the Smith decomposition theory as developed in Ref. [58], that allows to compute the vectors \mathbf{X} . The procedure can be briefly described as follows. The EBR matrix, which is in general a rectangular $n \times m$ matrix, can be Smith-decomposed in the form $\Delta = L \cdot \mathbf{EBR} \cdot R$, where L ($m \times m$) and R ($n \times n$) are unimodular matrices while Δ is a $n \times m$ matrix with nonzero entries only for the Δ_{ii} elements, with $i < r$, r being the rank of the EBR matrix. Using these new defined matrices the original problem for \mathbf{X} can be cast as

$$\Delta \cdot \mathbf{Y} = \mathbf{C}, \quad (7)$$

where $\mathbf{Y} = R^{-1}\mathbf{X}$ and $\mathbf{C} = L\mathbf{B}$. Then, the solution is

now expressed as

$$X = RY, \quad (8)$$

with Y having the explicit form

$$Y = (c_1/\Delta_{11}, c_1/\Delta_{11}, \dots, c_r/\Delta_{rr}, y_1, \dots, y_{N_{EBR}-1})^T, \quad (9)$$

where the parameters $y_1, \dots, y_{N_{EBR}-1}$ are integers which are free to be adjusted to obtain different solutions.

Applying this procedure to the vector \mathbf{B}_{MgCl_2} , the generic solution for this material will be

$$\mathbf{X} = (2 - y_1 - y_2, 3 - y_1 - y_2, 5 - 2y_1 - 2y_2, 6 - 2y_1 - 2y_2, -1 + y_1, -1 + 2y_1, y_2, y_2). \quad (10)$$

Next, we restrict \mathbf{X}_{MgCl_2} to correspond with the adequate atomic insulator, imposing all components to be positive integers or zero. In addition, we further limit the range of solutions discarding the cases $y_2 \neq 0$ since they imply that the charge centers are localized at unoccupied sites, the $3e$ WP. As we are interested in the OOAI phase, we only keep the solutions that involve EBRs induced from occupied WPs. Therefore, the final set of admissible solutions is

$$\mathbf{X}_{MgCl_2}^A = (1, 2, 3, 4, 0, 1, 0, 0), \quad (11)$$

$$\mathbf{X}_{MgCl_2}^B = (0, 1, 1, 2, 1, 3, 0, 0). \quad (12)$$

Hence, more than one decomposition will represent the same insulating state.

With the aim to characterize the orbital obstruction, we will introduce a more detailed classification for the insulating solutions. This is motivated by the concept of *movable* band representations and WPs [46]. This type of representation is defined as a combination of irreps that can be induced from a set of maximal WPs and can also be induced from the WPs that connect those maximal WPs in real space. Thus, for SG No. 164, we have two maximal WPs of interest, $1a$ and $2d$, and there is one non-maximal WP connecting them, the $6i$ WP, as depicted in the top left panel of Fig. 1. The set of irreps that can be interchangeably induced by these three WPs is given by

$$\begin{aligned} \Gamma : & \quad \bar{\Gamma}_4\bar{\Gamma}_5, \bar{\Gamma}_6\bar{\Gamma}_7, 2\bar{\Gamma}_8, 2\bar{\Gamma}_9. \\ M : & \quad 3\bar{M}_3\bar{M}_4, 3\bar{M}_5\bar{M}_6. \\ K : & \quad 2\bar{K}_4\bar{K}_5, 4\bar{K}_6. \end{aligned} \quad (13)$$

For this band representation, the charge centers can be adiabatically transported along the crystal structure respecting all the symmetries, thus the name movable BR [46]. It follows that this set cannot generate pinned BRs, which is a requisite for an obstructed phase to appear. In this context, a BR is said to be pinned if it is not movable. Therefore, in the subsequent analysis, this movable set will be subtracted from the insulator solutions obtained before. For the structures of interest, the movable

atomic insulator (MAI) state has two equivalent vector representations, one per each maximal WP:

$$\begin{aligned} \mathbf{X}_{MAI}^{1a} &= (1, 1, 2, 2, 0, 0, 0, 0). \\ \mathbf{X}_{MAI}^{2d} &= (0, 0, 0, 0, 1, 2, 0, 0). \end{aligned} \quad (14)$$

Now we compute the pinned solutions

$$\begin{aligned} \mathbf{X}_{MgCl_2}^A - \mathbf{X}_{MAI}^{1a}, \\ \mathbf{X}_{MgCl_2}^B - \mathbf{X}_{MAI}^{2d}, \end{aligned}$$

and obtain the same solution in both cases, which we denote as $\mathbf{X}_{MgCl_2}^O$, such that

$$\mathbf{X}_{MgCl_2}^O = (0, 1, 1, 2, 0, 1, 0, 0). \quad (15)$$

If this solution is inspected, we find that there are EBRs pinned to $1a$ and to $2d$ WPs. Nevertheless, all the EBRs from $1a$ have atomic support in real space, while the single EBR induced from $2d$ has partial support in real space. Thus, the OOAI phase in this material can be precisely identified as a mismatch of one EBR pinned at $2d$.

To characterize the anomaly, the number of electrons in the obstructed EBR must be quantified. For $MgCl_2$ there exist one electron in the $2d$ EBR for each Cl atom, which means that there is effectively only one mismatched state per Cl atom. Thus, the filling anomaly will consist of two obstructed states. This is in exact agreement with the energy spectrum of the finite geometry as presented in Fig. 4g.

ZrS₂

The next material to be studied is monolayer ZrS_2 . The motivation to present this structure is twofold. First, its energy gap is smaller than that of $MgCl_2$, which allows to compare the corresponding effect on the corner states. From the bulk band structure calculation, as depicted in Fig. 4b, the gap is of about 1.4 eV, which also yields a smaller energy gap in the finite structure. This is shown in Fig. 4h, where the energy spectrum of the flake geometry is presented. As expected, a filling anomaly can be observed. We note that in this case a different corner termination has been used, in order to probe for the presence of the filling anomaly and corner states in a different setting. The atomic configuration of the corner can be visualized in Fig. 4e.

From the energy spectrum in Fig. 4h, the corner states have merged with the upper states linked to the conduction band of the bulk. In fact, the band gap of ZrS_2 is over five times smaller than that of $MgCl_2$, and has the lowest band gap among the compounds presented in Fig. 4. For the sake of consistency with the rest of eigenvalue spectra presented in Fig. 4, the corner states are highlighted in a similar way as for the rest of panels. The LDOS at an energy range around the neutrality point is

sketched in Fig. 4e, showing that the corner localization still survives; as explained by the model, the support of these states comes almost exclusively from the $1a$ sites near the corners. This allows us to associate the obstructed phase of this material with the case where the energy ordering of the atomic limit implies that there are one or more EBRs coming from the $2d$ WP that are completely filled.

The second reason for highlighting this material is shown in Fig. 4h: the filling anomaly has now a different value involving four obstructed states. To explain this value, we follow the same procedure as in MgCl_2 , and only report here the final results. We first consider the atomic valence electronic configurations, which we set to be $3d^{10}4s^24p^64d^25s^2$ for Zr and $3s^23p^4$ for S. On the other hand, from the first-principles band structure calculation, the BR vector is

$$\mathbf{B}_{\text{ZrS}_2} = (1, 2, 4, 5, 5, 7, 4, 8). \quad (16)$$

The valid solutions are

$$\mathbf{X}_{\text{ZrS}_2}^A = (1, 2, 3, 4, 0, 1, 0, 0), \quad (17)$$

$$\mathbf{X}_{\text{ZrS}_2}^B = (0, 1, 1, 2, 1, 3, 0, 0). \quad (18)$$

After subtracting the MAI representations given by Eq. 14, the two solutions yield the same pinned configuration:

$$\mathbf{X}_{\text{ZrS}_2}^O = (0, 1, 1, 2, 0, 1, 0, 0). \quad (19)$$

Therefore, the pinned EBRs from the $1a$ WP have atomic support, while the pinned EBR from $2d$ WP has no support at all. This is different from the MgCl_2 case, since here both electrons of each S atom in the unit cell realize an obstruction. In consequence, a total of four electrons are mismatched, which traduces in a four-state filling anomaly. This is in agreement with the result obtained in the finite geometry calculation, and is a realization of a bulk-boundary correspondence.

SnS₂

Finally, we present a material showcasing the situation where the EBR at the Fermi level is induced by the $2d$ position, in order to discuss the differences with respect to the two preceding materials. For this purpose, monolayer SnS_2 is selected, whose electronic bulk band structure is plotted in Fig 4c. The band gap is of about 1.9 eV.

As can be deduced from what the model asserts, this case with half-filled EBR presents boundary responses that are coming from the valence band. This means that the filling anomaly will manifest in an under-filling with respect to the filling necessary for a gapped configuration. To verify this statement, the energy spectrum is computed and presented in Fig. 4i, which is in agreement with the physical picture provided by the model. There is a deficit of eight electrons at the neutrality point. In

our case, the filling anomaly is only well defined modulo 12, since the band representation corresponding to the MAI (see Eq. 14) involves 12 electrons and, by definition, they cannot be pinned to any WP in real space. Thus, the anomaly of SnS_2 will be equivalent to an obstruction of 4 electrons ($-8 \bmod 12$).

To check this, we apply the Smith decomposition procedure as in the previous cases. For Sn we use the valence electronic configuration $5s^25p^2$ and for S we employ $3s^23p^4$. The symmetry data vector is

$$\mathbf{B}_{\text{SnS}_2} = (3, 1, 6, 3, 9, 4, 5, 8). \quad (20)$$

And the valid solutions are

$$\mathbf{X}_{\text{SnS}_2}^A = (3, 1, 5, 2, 0, 1, 0, 0), \quad (21)$$

$$\mathbf{X}_{\text{SnS}_2}^B = (2, 0, 3, 0, 1, 3, 0, 0). \quad (22)$$

Subtracting the appropriate MAI representation given by Eq. 14 to the above solutions, the outcome is the same for both cases and is given by

$$\mathbf{X}_{\text{SnS}_2}^O = (2, 0, 3, 0, 0, 1, 0, 0). \quad (23)$$

It is straightforward to see that there is a pinned EBR coming from the $2d$ WP, which does not have support in real space. This is due to the fact that the real space atomic occupation locates the electrons at the external shell of the Sn atoms ($5s^25p^2$). Hence, the mismatch will be of two electrons per S atom, resulting in an overall filling anomaly of four, which coincides with the finite geometry calculation.

The character of the boundary states at the energy range where the anomaly is realized can be explored in terms of the corresponding LDOS for the finite geometry. This information is presented in Fig. 4f, illustrating that the states that contribute to the vicinity of the neutrality point come from the $2d$ sites. This is expected, because the edge states are induced by the upper bands of the system (see Section III D), and these upper bands for SnS_2 are induced from the $2d$ WP. In addition, we find here that the corner and edge states mix and yield a LDOS contribution that extends along a portion of the flake boundary. These states can be directly related to bands with fragile topology, which are feasible in this SG, and that for this monolayer occur right at the top of the valence manifold [59].

V. DISCUSSION

In this work we have identified a topological phase realized as an obstructed atomic limit due to the orbital character and energy ordering for systems within SG No. 164. Using the TQC formalism, we have provided a detailed characterization of the mechanism that allows the emergence of this orbital obstruction. In addition, we have discussed the effect of this phenomenon in a finite geometry, leading to a filling anomaly. Remarkably, this

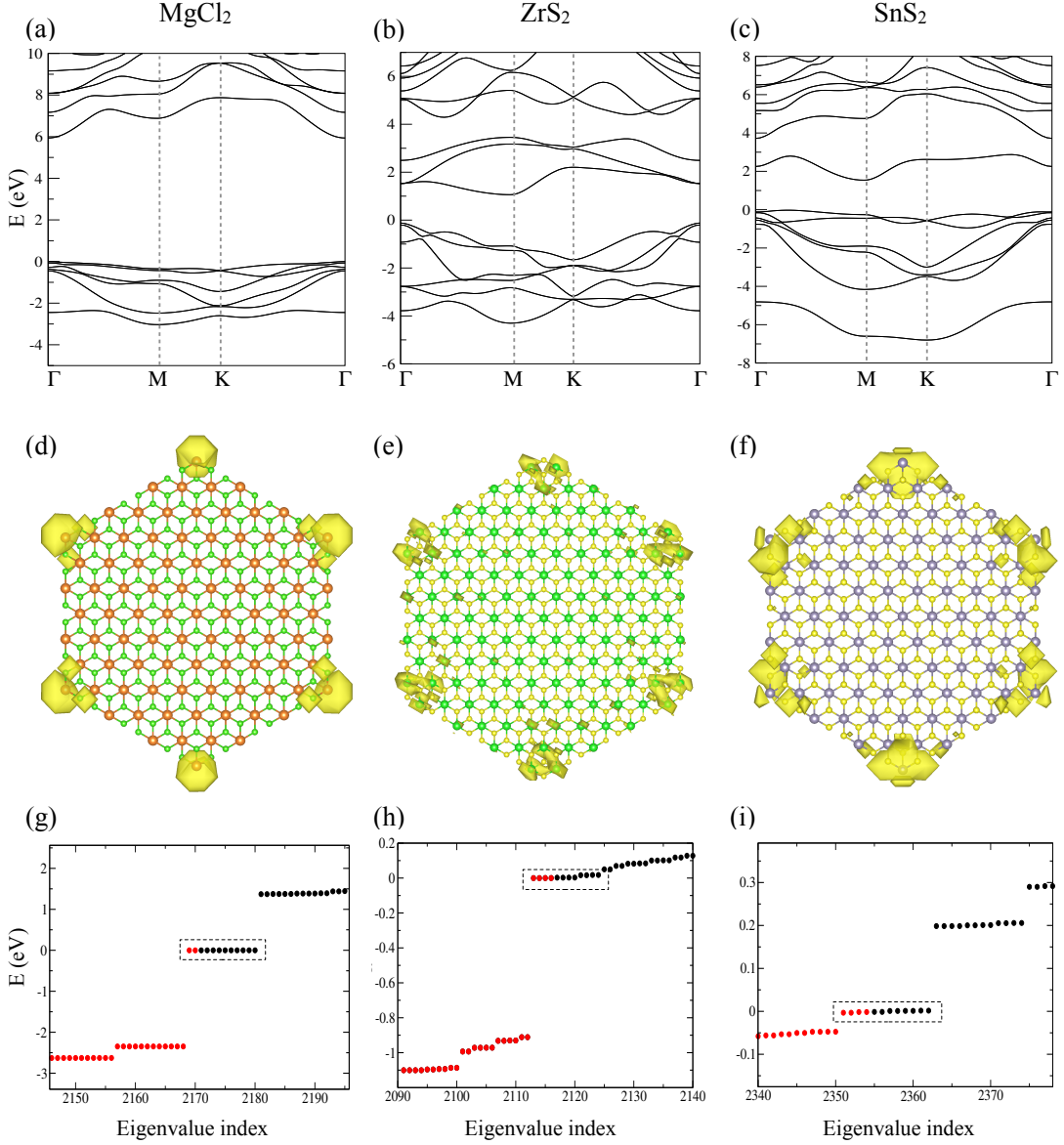


FIG. 4. Top panels (a - c): band structures of the three highlighted MX₂ monolayers belonging to SG No. 164. Middle panels (d - f): LDOS for MgCl₂, ZrS₂ and SnS₂ hexagonal flakes. Bottom panels (g - i): corresponding eigenvalue spectra of the hexagonal flakes depicted in the previous panels. The corner states are highlighted by enclosing them in rectangular regions near the neutrality point.

filling anomaly is robust and does not depend on the presence of edge states in the system. Moreover, using a complementary minimal six-band model, the conditions for the occurrence of edge states in both ribbon and finite systems have been discussed.

The exemplary materials presented in the previous section constitute realistic platforms for exploring the con-

sequences of topological orbital obstruction. As this phenomena depends on the orbital character of the constituents and on the energetic ordering that is realized in each material, this study can be readily extended to encompass the entire family of MX₂-type materials within SG No. 164. We present a summary of the calculations of the type of bulk orbital obstruction for a set of mono-

Filling anomaly value	Material
2	CdCl ₂ , CdBr ₂ , CdI ₂ , CdF ₂
	RuCl ₂ , RuBr ₂ , RuI ₂
	ZnCl ₂ , ZnBr ₂ , ZnI ₂
	MgCl ₂ , MgBr ₂ , MgI ₂
	CaBr ₂ , CaI ₂
	SrBr ₂ , SrI ₂
	OsBr ₂ , OsI ₂
	BaBr ₂ , BaI ₂
	PbBr ₂ , PbI ₂
	ZrF ₂ , HgF ₂ , PdCl ₂ , SnI ₂ , GeI ₂
	4
HfO ₂ , HfS ₂ , HfSe ₂	
PtO ₂ , PtS ₂ , PtSe ₂	
ZrO ₂ , ZrS ₂ , ZrSe ₂	
NiO ₂ , NiS ₂	
PbO ₂ , PbS ₂	
SnO ₂ , SnS ₂	
GeO ₂ , GeS ₂	
SiSe ₂	

TABLE II. Filling anomaly value for the studied materials. Recall that this value is well defined only modulo 12.

layers extracted from the database in [34, 35] in Table II, where the magnitude of the filling anomaly is reported for each material. Moreover, since our analysis is based on general TQC algorithms, it can also be extended to other SG No. 164 materials, as well as to other space groups.

Our findings clarify and complement previous results on nontrivial topological properties. In particular, comparing with Ref. [55], we found a different mechanism for the higher-order response of the hexagonal finite geometries, which best accounts for all possible results for the family of materials with SG No. 164. Thus, if for example, the theory of symmetry-indicator invariants is applied to materials like MgCl₂, we encounter an incorrect value for the filling anomaly, since this invariant does not account for the orbital obstruction as the main responsible of the nontrivial phase for halogen-based monolayers. On the other hand, considering Ref. [22], we find similar conclusions related to materials with a half-filled EBR coming from the $2d$ WP, for instance SnS₂, which is also reported in the aforementioned work. The novelty of our analysis is that we identify a new effect related to these orbital-obstructed phases: a filling anomaly. We also extend the nontrivial behavior to cases that were previously overlooked, such as materials with completely filled EBRs coming from an atomic limit related to the $2d$ WP, which include several monolayer transition metal dichalcogenides.

Regarding the formal interpretation of the orbital obstructed phases discussed in this work, following Ref. [60], the solutions that constitute an OOAI are affine monoids. In particular, the affine monoids of interest have a trivial Hilbert basis and can be defined as the monoids that arise when from the complete EBR monoid

we subtract the monoid of the EBRs with electronic support. This is similar to the case of an obstructed atomic insulator, as presented in Ref. [61].

It is also interesting to mention the possible future routes for orbital-obstructed topology. As we briefly mentioned in the previous section, fragile topology can be present in an indirect form for the materials with a half-filled EBR from $2d$ WP [59]. The role that this kind of topology plays in the boundary responses is of great interest since there are few cases of electronic systems where fragility leads to measurable phenomena.

Another appealing research line is related to correlation effects in these systems. In particular, many of the materials reported here are known to realize the so-called charge-transfer insulating state [62, 63], which entails states where the low energy excitations of the material are related to an unexpected electron transfer from the X atoms to the M atoms. This process is well-established for example in bulk three-dimensional transition metal oxides such as NiO [64], but it is less studied in layered transition metal dichalcogenide systems and other samples where M is an alkali metal like Mg, or a group IV element like Ge or Sn. Therefore, it would be intriguing to characterize how the orbital obstruction is affected when considering electronic correlation effects.

ACKNOWLEDGEMENTS

We acknowledge the financial support of the Agencia Estatal de Investigación of Spain under grant PID2022-136285NB-C31 and from the Comunidad de Madrid through the (MAD2D-CM)-UCM5 project, funded by the Recovery, Transformation and Resilience Plan, and by NextGenerationEU from the European Union. O.A.G acknowledges funding from European Union NextGenerationEU/PRTR project Consolidación Investigadora CNS2022-136025. S.B. acknowledges the support of the Postdoctoral Grant from the Universidad Técnica Federico Santa María. M. P. acknowledges the financial support of Chilean FONDECYT by grant 1211913. S.B acknowledges the support of the postdoctoral position at Universidad Técnica Federico Santa María. Finally, we thank the Centro de Supercomputación de Galicia, CESGA, (www.cesga.es, Santiago de Compostela, Spain) and Supercomputación Castilla y León (SCAYLE) for providing access to their supercomputing facilities.

APPENDIX

Computational details

Electronic structure calculations for all materials were carried out by means of the Quantum ESPRESSO first-

principles code [65, 66] using the generalized gradient approximation (GGA) and Perdew–Burke–Ernzerhof (PBE) exchange–correlation functional. Spin-orbit coupling was considered throughout the self-consistent calculations in all cases. A kinetic energy wavefunction cutoff of 100 Ry and a $8 \times 8 \times 1$ Monkhorst-Pack reciprocal space grid were employed for all calculations. All structures were relaxed until the forces were under 0.001 eV/Å. The initial crystal structures were obtained from the Computational 2D Materials Database (C2DB) [34, 35] and checked against the Topological Materials Database [1, 8, 67]. Afterwards, the irreducible representations were obtained using the IrRep code [68]. For the flake calculations, the SIESTA code [69, 70] was used, considering the same GGA-PBE approximation and spin-orbit coupling. The flake and ribbon numerical calculations based on the tight-binding model were carried using the Kwant package [71].

Tight-binding model functions

$$F(r_\alpha, r_\beta) = \sum_{m \in \{k_x, k_y, k_x + k_y\}} r_\alpha \cos m + i r_\beta \sin m,$$

where α and $\beta \in \{1, 2, 4\}$.

$$G(r_3) = \frac{2}{\sqrt{3}} r_3 [i \sin k_x + \omega^* \sin k_y + \omega \sin(k_x + k_y)].$$

where $\omega = e^{i\pi/6}$.

$$L(\xi) = \xi (z_1^* + z_2 + z_3).$$

$$M(\xi) = \xi (\phi^* z_1^* + \phi z_2 - z_3).$$

$$\tilde{M}(\xi) = -\xi (\phi z_1^* + \phi^* z_2 + z_3).$$

$$\tilde{T}(\xi) = -\xi (\phi^* z_1 + \phi z_2^* - z_3^*).$$

- [1] M. G. Vergniory, L. Elcoro, C. Felser, N. Regnault, B. A. Bernevig, and Z. Wang, A complete catalogue of high-quality topological materials, *Nature* **566**, 480 (2019).
- [2] T. Zhang, Y. Jiang, Z. Song, H. Huang, Y. He, Z. Fang, H. Weng, and C. Fang, Catalogue of topological electronic materials, *Nature* **566**, 475 (2019).
- [3] B. J. Wieder, B. Bradlyn, J. Cano, Z. Wang, M. G. Vergniory, L. Elcoro, A. A. Soluyanov, C. Felser, T. Neupert, N. Regnault, and B. A. Bernevig, Topological materials discovery from crystal symmetry, *Nature Reviews Materials* **7**, 196 (2022).
- [4] F. Schindler, Z. Wang, M. G. Vergniory, A. M. Cook, A. Murani, S. Sengupta, A. Y. Kasumov, R. Deblock, S. Jeon, I. Drozdov, H. Bouchiat, S. Guéron, A. Yazdani, B. A. Bernevig, and T. Neupert, Higher-order topology in bismuth, *Nature Physics* **14**, 918 (2018).
- [5] F. Schindler, A. M. Cook, M. G. Vergniory, Z. Wang, S. S. P. Parkin, B. A. Bernevig, and T. Neupert, Higher-order topological insulators, *Science Advances* **4**,

Here, $\phi = e^{i\pi/3}$ and

$$z_1 = e^{i/3(2k_x + k_y)},$$

$$z_2 = e^{i/3(k_x - k_y)},$$

$$z_3 = e^{i/3(k_x + 2k_y)}.$$

EBR matrix for space group $\bar{P}3m1$ monolayers

As stated in Section IV, we perform a Topological Quantum Chemistry analysis of the valence bands of three different monolayers belonging to space group $\bar{P}3m1$. The EBR matrix, which is the same for all $\bar{P}3m1$ monolayers, is detailed in the following.

$$\begin{pmatrix} 1 & 0 & 0 & 0 & 1 & 0 & 1 & 0 \\ 0 & 1 & 0 & 0 & 1 & 0 & 0 & 1 \\ 0 & 0 & 1 & 0 & 0 & 1 & 2 & 0 \\ 0 & 0 & 0 & 1 & 0 & 1 & 0 & 2 \\ 1 & 0 & 1 & 0 & 1 & 1 & 1 & 2 \\ 0 & 1 & 0 & 1 & 1 & 1 & 2 & 1 \\ 1 & 1 & 0 & 0 & 0 & 1 & 1 & 1 \\ 0 & 0 & 1 & 1 & 2 & 1 & 2 & 2 \end{pmatrix}. \quad (24)$$

Correspondingly, the Δ matrix that obeys $\Delta = L \cdot EBR \cdot R$ is stated below. More information on the EBR matrix can be found in Section IV, Eqs. 6 - 9.

$$\begin{pmatrix} 1 & 0 & 0 & 0 & 0 & 0 & 0 & 0 \\ 0 & 1 & 0 & 0 & 0 & 0 & 0 & 0 \\ 0 & 0 & 1 & 0 & 0 & 0 & 0 & 0 \\ 0 & 0 & 0 & 1 & 0 & 0 & 0 & 0 \\ 0 & 0 & 0 & 0 & 1 & 0 & 0 & 0 \\ 0 & 0 & 0 & 0 & 0 & 2 & 0 & 0 \\ 0 & 0 & 0 & 0 & 0 & 0 & 0 & 0 \\ 0 & 0 & 0 & 0 & 0 & 0 & 0 & 0 \end{pmatrix}. \quad (25)$$

- [6] W. A. Benalcazar, B. A. Bernevig, and T. L. Hughes, Quantized electric multipole insulators, *Science* **357**, 61 (2017).
- [7] Y. Han, C. Cui, X.-P. Li, T.-T. Zhang, Z. Zhang, Z.-M. Yu, and Y. Yao, Cornertronics in two-dimensional second-order topological insulators, *Physical Review Letters* **133**, 10.1103/physrevlett.133.176602 (2024).
- [8] B. Bradlyn, L. Elcoro, J. Cano, M. G. Vergniory, Z. Wang, C. Felser, M. I. Aroyo, and B. A. Bernevig, Topological quantum chemistry, *Nature* **547**, 298 (2017).
- [9] J. Cano, B. Bradlyn, Z. Wang, L. Elcoro, M. G. Vergniory, C. Felser, M. I. Aroyo, and B. A. Bernevig, Building blocks of topological quantum chemistry: Elementary band representations, *Physical Review B* **97**, 035139 (2018).
- [10] H. C. Po, A. Vishwanath, and H. Watanabe, Symmetry-based indicators of band topology in the 230 space groups, *Nature Communications* **8**, 50 (2017).

- [11] E. Khalaf, H. C. Po, A. Vishwanath, and H. Watanabe, Symmetry Indicators and Anomalous Surface States of Topological Crystalline Insulators, *Physical Review X* **8**, 031070 (2018).
- [12] H. C. Po, Symmetry indicators of band topology, *Journal of Physics: Condensed Matter* **32**, 263001 (2020).
- [13] J. Kruthoff, J. de Boer, J. van Wezel, C. L. Kane, and R.-J. Slager, Topological classification of crystalline insulators through band structure combinatorics, *Physical Review X* **7**, 041069 (2017).
- [14] R.-J. Slager, A. Mesaros, V. Juričić, and J. Zaenen, The space group classification of topological band-insulators, *Nature Physics* **9**, 98–102 (2012).
- [15] J. Cano and B. Bradlyn, Band Representations and Topological Quantum Chemistry, *Annual Review of Condensed Matter Physics* **12**, 225 (2021).
- [16] Y. Xu, L. Elcoro, Z.-D. Song, M. G. Vergniory, C. Felser, S. S. P. Parkin, N. Regnault, J. L. Mañes, and B. A. Bernevig, Filling-enforced obstructed atomic insulators, *Physical Review B* **109**, 165139 (2024).
- [17] Y. Xu, L. Elcoro, G. Li, Z.-D. Song, N. Regnault, Q. Yang, Y. Sun, S. Parkin, C. Felser, and B. A. Bernevig, Three-Dimensional Real Space Invariants, Obstructed Atomic Insulators and A New Principle for Active Catalytic Sites (2021), arXiv:2111.02433 [cond-mat].
- [18] G. Li, Y. Xu, Z. Song, Q. Yang, Y. Zhang, J. Liu, U. Gupta, V. Süß, Y. Sun, P. Sessi, S. S. P. Parkin, B. A. Bernevig, and C. Felser, Obstructed Surface States as the Descriptor for Predicting Catalytic Active Sites in Inorganic Crystalline Materials, *Advanced Materials* **34**, 2201328 (2022).
- [19] W. A. Benalcazar, T. Li, and T. L. Hughes, Quantization of fractional corner charge in C_n -symmetric higher-order topological crystalline insulators, *Physical Review B* **99**, 245151 (2019).
- [20] F. Schindler, M. Brzezińska, W. A. Benalcazar, M. Iraola, A. Bouhon, S. S. Tsirkin, M. G. Vergniory, and T. Neupert, Fractional corner charges in spin-orbit coupled crystals, *Physical Review Research* **1**, 033074 (2019).
- [21] J. Gao, Y. Qian, H. Jia, Z. Guo, Z. Fang, M. Liu, H. Weng, and Z. Wang, Unconventional materials: The mismatch between electronic charge centers and atomic positions, *Science Bulletin* **67**, 598 (2022).
- [22] H. Sheng, Y. Xie, Q. Wu, H. Weng, X. Dai, B. A. Bernevig, Z. Fang, and Z. Wang, Majorana corner modes in unconventional monolayers of the 1T-PtSe₂ family, *Physical Review B* **110**, 035151 (2024).
- [23] U. Petralanda, Y. Jiang, B. A. Bernevig, N. Regnault, and L. Elcoro, Two-dimensional topological quantum chemistry and catalog of topological materials (2024).
- [24] S. Mañas-Valero, V. García-López, A. Cantarero, and M. Galbiati, Raman Spectra of ZrS₂ and ZrSe₂ from Bulk to Atomically Thin Layers, *Applied Sciences* **6**, 264 (2016).
- [25] G. Ye, Y. Gong, S. Lei, Y. He, B. Li, X. Zhang, Z. Jin, L. Dong, J. Lou, R. Vajtai, W. Zhou, and P. M. Ajayan, Synthesis of large-scale atomic-layer SnS₂ through chemical vapor deposition, *Nano Research* **10**, 2386 (2017).
- [26] P. Tsipas, D. Tsoutsou, S. Fragkos, R. Sant, C. Alvarez, H. Okuno, G. Renaud, R. Alcotte, T. Baron, and A. Dimoulas, Massless Dirac Fermions in ZrTe₂ Semimetal Grown on InAs(111) by van der Waals Epitaxy, *ACS Nano* **12**, 1696 (2018).
- [27] C. Xu, B. Li, W. Jiao, W. Zhou, B. Qian, R. Sankar, N. D. Zhigadlo, Y. Qi, D. Qian, F.-C. Chou, and X. Xu, Topological Type-II Dirac Fermions Approaching the Fermi Level in a Transition Metal Dichalcogenide NiTe₂, *Chemistry of Materials* **30**, 4823 (2018).
- [28] K. Zhang, M. Yan, H. Zhang, H. Huang, M. Arita, Z. Sun, W. Duan, Y. Wu, and S. Zhou, Experimental evidence for type-II Dirac semimetal in PtSe₂, *Physical Review B* **96**, 125102 (2017).
- [29] Y. Wang, L. Li, W. Yao, S. Song, J. T. Sun, J. Pan, X. Ren, C. Li, E. Okunishi, Y.-Q. Wang, E. Wang, Y. Shao, Y. Y. Zhang, H.-t. Yang, E. F. Schwier, H. Iwasawa, K. Shimada, M. Taniguchi, Z. Cheng, S. Zhou, S. Du, S. J. Pennycook, S. T. Pantelides, and H.-J. Gao, Monolayer PtSe₂, a New Semiconducting Transition-Metal-Dichalcogenide, Epitaxially Grown by Direct Selenization of Pt, *Nano Letters* **15**, 4013 (2015).
- [30] Q.-Q. Yuan, F. Zheng, Z.-Q. Shi, Q.-Y. Li, Y.-Y. Lv, Y. Chen, P. Zhang, and S.-C. Li, Direct Growth of van der Waals Tin Diodide Monolayers, *Advanced Science* **8**, 2100009 (2021).
- [31] S. Sinha, T. Zhu, A. France-Lanord, Y. Sheng, J. C. Grossman, K. Porfyrakis, and J. H. Warner, Atomic structure and defect dynamics of monolayer lead iodide nanodisks with epitaxial alignment on graphene, *Nature Communications* **11**, 823 (2020).
- [32] E. Chen, W. Xu, J. Chen, and J. H. Warner, 2D layered noble metal dichalcogenides (Pt, Pd, Se, S) for electronics and energy applications, *Materials Today Advances* **7**, 100076 (2020).
- [33] L. Liu, D. Zemlyanov, and Y. P. Chen, Epitaxial growth of monolayer PdTe₂ and patterned PtTe₂ by direct tellurization of Pd and Pt surfaces, *2D Materials* **8**, 045033 (2021).
- [34] S. Haastrup, M. Strange, M. Pandey, T. Deilmann, P. S. Schmidt, N. F. Hinsche, M. N. Gjerding, D. Torelli, P. M. Larsen, A. C. Riis-Jensen, J. Gath, K. W. Jacobsen, J. J. Mortensen, T. Olsen, and K. S. Thygesen, The Computational 2D Materials Database: High-throughput modeling and discovery of atomically thin crystals, *2D Materials* **5**, 042002 (2018).
- [35] M. N. Gjerding, A. Taghizadeh, A. Rasmussen, S. Ali, F. Bertoldo, T. Deilmann, N. R. Knøsgaard, M. Kruse, A. H. Larsen, S. Manti, T. G. Pedersen, U. Petralanda, T. Skovhus, M. K. Svendsen, J. J. Mortensen, T. Olsen, and K. S. Thygesen, Recent progress of the Computational 2D Materials Database (C2DB), *2D Materials* **8**, 044002 (2021).
- [36] M. I. Aroyo, J. M. Perez-Mato, C. Capillas, E. Kroumova, S. Ivantchev, G. Madariaga, A. Kirov, and H. Wondratschek, Bilbao Crystallographic Server: I. Databases and crystallographic computing programs, *Zeitschrift für Kristallographie - Crystalline Materials* **221**, 15 (2006).
- [37] L. Elcoro, B. Bradlyn, Z. Wang, M. G. Vergniory, J. Cano, C. Felser, B. A. Bernevig, D. Orobengoa, G. de la Flor, and M. I. Aroyo, Double crystallographic groups and their representations on the Bilbao Crystallographic Server, *Journal of Applied Crystallography* **50**, 1457 (2017).
- [38] M. I. Aroyo, A. Kirov, C. Capillas, J. M. Perez-Mato, and H. Wondratschek, Bilbao Crystallographic Server. II. Representations of crystallographic point groups and space groups, *Acta Crystallographica Section A Foundations of Crystallography* **62**, 115 (2006).

- [39] M. Aroyo, J. Perez-Mato, D. Orobengoa, E. Tasci, G. De La Flor, and A. Kirov, Crystallography online: Bilbao crystallographic server, Bulgarian Chemical Communications **43**, 183 (2011).
- [40] M. S. Dresselhaus, G. Dresselhaus, and A. Jorio, eds., *Group Theory*, SpringerLink Bücher (Springer Berlin Heidelberg, Berlin, Heidelberg, 2008).
- [41] Z. Zhang, Z.-M. Yu, G.-B. Liu, and Y. Yao, Magnetictb: A package for tight-binding model of magnetic and non-magnetic materials, Computer Physics Communications **270**, 108153 (2022).
- [42] J. Cano, B. Bradlyn, Z. Wang, L. Elcoro, M. G. Vergniory, C. Felser, M. I. Aroyo, and B. A. Bernevig, Topology of Disconnected Elementary Band Representations, Physical Review Letters **120**, 266401 (2018).
- [43] H. C. Po, H. Watanabe, and A. Vishwanath, Fragile topology and wannier obstructions, Physical Review Letters **121**, 126402 (2018).
- [44] B. Bradlyn, Z. Wang, J. Cano, and B. A. Bernevig, Disconnected elementary band representations, fragile topology, and Wilson loops as topological indices: An example on the triangular lattice, Physical Review B **99**, 045140 (2019).
- [45] W. A. Benalcazar, B. A. Bernevig, and T. L. Hughes, Electric multipole moments, topological multipole moment pumping, and chiral hinge states in crystalline insulators, Physical Review B **96**, 245115 (2017).
- [46] E. Khalaf, W. A. Benalcazar, T. L. Hughes, and R. Queiroz, Boundary-obstructed topological phases, Physical Review Research **3**, 013239 (2021).
- [47] G. F. Lange, A. Bouhon, and R.-J. Slager, Subdimensional topologies, indicators, and higher order boundary effects, Phys. Rev. B **103**, 195145 (2021).
- [48] Z. Wang, B. J. Wieder, J. Li, B. Yan, and B. A. Bernevig, Higher-Order Topology, Monopole Nodal Lines, and the Origin of Large Fermi Arcs in Transition Metal Dichalcogenides XTe_2 ($X = Mo, W$), Physical Review Letters **123**, 186401 (2019).
- [49] S. Kooi, G. Van Miert, and C. Ortix, The bulk-corner correspondence of time-reversal symmetric insulators, npj Quantum Materials **6**, 1 (2021).
- [50] V. Nuñez, S. Bravo, J. D. Correa, L. Chico, and M. Pacheco, Higher-order obstructed atomic insulator phase in pentagonal monolayer $PdSe_2$, 2D Materials **11**, 015015 (2023).
- [51] M. Costa, B. Focassio, L. M. Canonico, T. P. Cysne, G. R. Schleder, R. B. Muniz, A. Fazzio, and T. G. Rappoport, Connecting Higher-Order Topology with the Orbital Hall Effect in Monolayers of Transition Metal Dichalcogenides, Physical Review Letters **130**, 116204 (2023).
- [52] S. Qian, G.-B. Liu, C.-C. Liu, and Y. Yao, Cn -symmetric higher-order topological crystalline insulators in atomically thin transition metal dichalcogenides, Physical Review B **105**, 045417 (2022).
- [53] J. Zeng, H. Liu, H. Jiang, Q.-F. Sun, and X. C. Xie, Multiorbital model reveals a second-order topological insulator in 1 H transition metal dichalcogenides, Physical Review B **104**, L161108 (2021).
- [54] G. Liu, H. Jiang, Z. Guo, X. Zhang, L. Jin, C. Liu, and Y. Liu, Magnetic Second-Order Topological Insulators in 2H-Transition Metal Dichalcogenides, Advanced Science **10**, 2301952 (2023).
- [55] G. Long, M. Pan, H. Zeng, and H. Huang, Second-order topological insulators in two-dimensional monolayers of the 1T-phase $PtSe_2$ material class, Phys. Rev. Mater. **8**, 044203 (2024).
- [56] S. Manna, S. Nandy, and B. Roy, Higher-order topological phases on fractal lattices, Phys. Rev. B **105**, L210301 (2022).
- [57] M. Jung, Y. Yu, and G. Shvets, Exact higher-order bulk-boundary correspondence of corner-localized states, Physical Review B **104**, 195437 (2021).
- [58] L. Elcoro, Z. Song, and B. A. Bernevig, Application of induction procedure and Smith decomposition in calculation and topological classification of electronic band structures in the 230 space groups, Physical Review B **102**, 035110 (2020).
- [59] O. Arroyo-Gascón, S. Bravo, L. Chico, and M. Pacheco, Fractional corner charges in threefold-symmetric two-dimensional materials with fragile topology, Phys. Rev. Res. **7**, 023282 (2025).
- [60] Z.-D. Song, L. Elcoro, Y.-F. Xu, N. Regnault, and B. A. Bernevig, Fragile Phases as Affine Monoids: Classification and Material Examples, Physical Review X **10**, 031001 (2020).
- [61] Z. Zhang, Y. X. Zhao, Y. Yao, and S. A. Yang, Hilbert band complexes and their applications, Phys. Rev. B **111**, 075154 (2025).
- [62] D. I. Khomskii, *Transition Metal Compounds*, 1st ed. (Cambridge University Press, 2014).
- [63] A. V. Ushakov, S. V. Streltsov, and D. I. Khomskii, Crystal field splitting in correlated systems with negative charge-transfer gap, Journal of Physics: Condensed Matter **23**, 445601 (2011).
- [64] J. Kuneš, V. I. Anisimov, S. L. Skornyakov, A. V. Lukoyanov, and D. Vollhardt, NiO: Correlated Band Structure of a Charge-Transfer Insulator, Physical Review Letters **99**, 156404 (2007).
- [65] P. Giannozzi, S. Baroni, N. Bonini, M. Calandra, R. Car, C. Cavazzoni, D. Ceresoli, G. L. Chiarotti, M. Cococcioni, I. Dabo, A. D. Corso, S. de Gironcoli, S. Fabris, G. Fratesi, R. Gebauer, U. Gerstmann, C. Gougoussis, A. Kokalj, M. Lazzeri, L. Martin-Samos, N. Marzari, F. Mauri, R. Mazzarello, S. Paolini, A. Pasquarello, L. Paulatto, C. Sbraccia, S. Scandolo, G. Sclauzero, A. P. Seitsonen, A. Smogunov, P. Umari, and R. M. Wentzcovitch, QUANTUM ESPRESSO: A modular and open-source software project for quantum simulations of materials, Journal of Physics: Condensed Matter **21**, 395502 (2009).
- [66] P. Giannozzi, O. Andreussi, T. Brumme, O. Bunau, M. B. Nardelli, M. Calandra, R. Car, C. Cavazzoni, D. Ceresoli, M. Cococcioni, N. Colonna, I. Carnimeo, A. D. Corso, S. de Gironcoli, P. Delugas, R. A. DiStasio, A. Ferretti, A. Floris, G. Fratesi, G. Fugallo, R. Gebauer, U. Gerstmann, F. Giustino, T. Gorni, J. Jia, M. Kawamura, H.-Y. Ko, A. Kokalj, E. Küçükbenli, M. Lazzeri, M. Marsili, N. Marzari, F. Mauri, N. L. Nguyen, H.-V. Nguyen, A. Otero-de-la-Roza, L. Paulatto, S. Poncé, D. Rocca, R. Sabatini, B. Santra, M. Schlipf, A. P. Seitsonen, A. Smogunov, I. Timrov, T. Thonhauser, P. Umari, N. Vast, X. Wu, and S. Baroni, Advanced capabilities for materials modelling with Quantum ESPRESSO, Journal of Physics: Condensed Matter **29**, 465901 (2017).
- [67] M. G. Vergniory, B. J. Wieder, L. Elcoro, S. S. P. Parkin, C. Felser, B. A. Bernevig, and N. Regnault, All topolog-

- ical bands of all nonmagnetic stoichiometric materials, *Science* **376**, eabg9094 (2022).
- [68] M. Iraola, J. L. Mañes, B. Bradlyn, M. K. Horton, T. Neupert, M. G. Vergniory, and S. S. Tsirkin, IrRep: Symmetry eigenvalues and irreducible representations of ab initio band structures, *Computer Physics Communications* **272**, 108226 (2022).
- [69] J. M. Soler, E. Artacho, J. D. Gale, A. García, J. Junquera, P. Ordejón, and D. Sánchez-Portal, The SIESTA method for ab initio order-N materials simulation, *Journal of Physics: Condensed Matter* **14**, 2745 (2002).
- [70] A. García, N. Papior, A. Akhtar, E. Artacho, V. Blum, E. Bosoni, P. Brandimarte, M. Brandbyge, J. I. Cerdá, F. Corsetti, R. Cuadrado, V. Dikan, J. Ferrer, J. Gale, P. García-Fernández, V. M. García-Suárez, S. García, G. Huhs, S. Illera, R. Korytár, P. Koval, I. Lebedeva, L. Lin, P. López-Tarifa, S. G. Mayo, S. Mohr, P. Ordejón, A. Postnikov, Y. Pouillon, M. Pruneda, R. Robles, D. Sánchez-Portal, J. M. Soler, R. Ullah, V. W.-z. Yu, and J. Junquera, Siesta: Recent developments and applications, *The Journal of Chemical Physics* **152**, 204108 (2020).
- [71] C. W. Groth, M. Wimmer, A. R. Akhmerov, and X. Waintal, Kwant: a software package for quantum transport, *New Journal of Physics* **16**, 063065 (2014).